Supporting Information for "Rift zone architecture and inflation-driven seismicity of Mauna Loa volcano"

John D. Wilding[1], Zachary E. Ross[1]

[1]Seismological Laboratory, California Institute of Technology

Contents of this file

1. Figures S1 to S8

Introduction This supporting information file contains 8 figures to supplement the main text of the article.

References

Sherrod, D. R., Sinton, J. M., Watkins, S. E., & Brunt, K. M. (2021). *Geologic map of the State of Hawaii* (USGS Numbered Series No. 3143). Reston, VA: U.S. Geological Survey. Retrieved 2022-11-03, from http://pubs.er.usgs.gov/publication/sim3143 doi: 10.3133/sim3143

Varugu, B., & Amelung, F. (2021, May). Southward growth of Mauna Loa's dike-like magma body driven by topographic stress. *Scientific Reports*, *11*(1), 9816. Retrieved 2021-09-02, from https://www.nature.com/articles/s41598-021-89203-6 doi: 10.1038/s41598-021-89203-6

Wolfe (compiler), E. W., & Morris, J. (1996). *Geologic map of the Island of Hawaii* (Tech. Rep. No. 2524-A). U.S. Geological Survey. Retrieved 2022-11-03, from https://pubs.er.usgs.gov/publication/i2524A (ISBN: 9780607860825 Publication Title: IMAP) doi: 10.3133/i2524A

Zaliapin, I., & Ben-Zion, Y. (2013). Earthquake clusters in southern California I: Identification and stability. *Journal of Geophysical Research: Solid Earth*, *118*(6), 2847–2864. Retrieved 2021-01-19, from https://agupubs.onlinelibrary.wiley.com/doi/abs/10.1002/jgrb.50179 doi: https://doi.org/10.1002/jgrb.50179

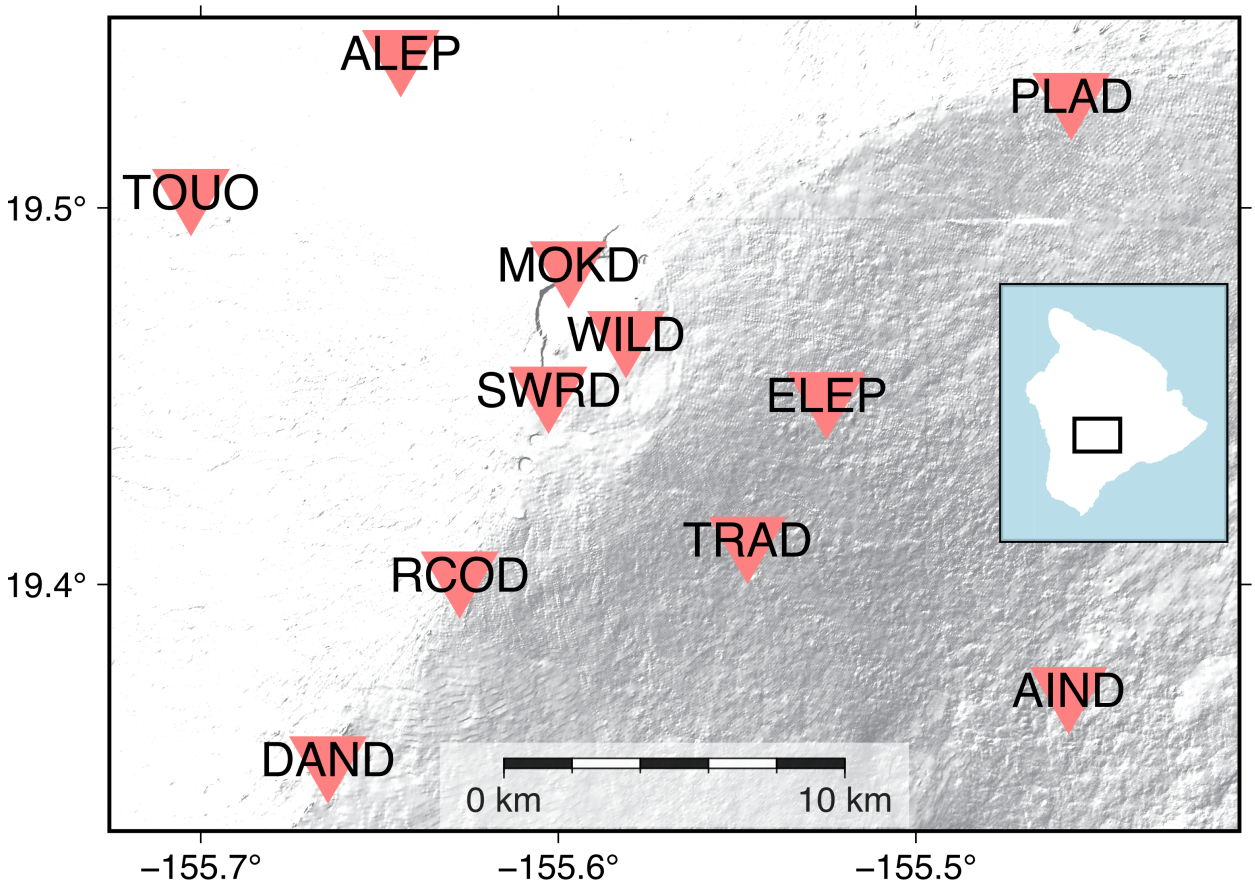

Figure S1. Map and labels of seismic stations from the HV network used in this study. Inset: location of our study region on the Island of Hawai‘i.

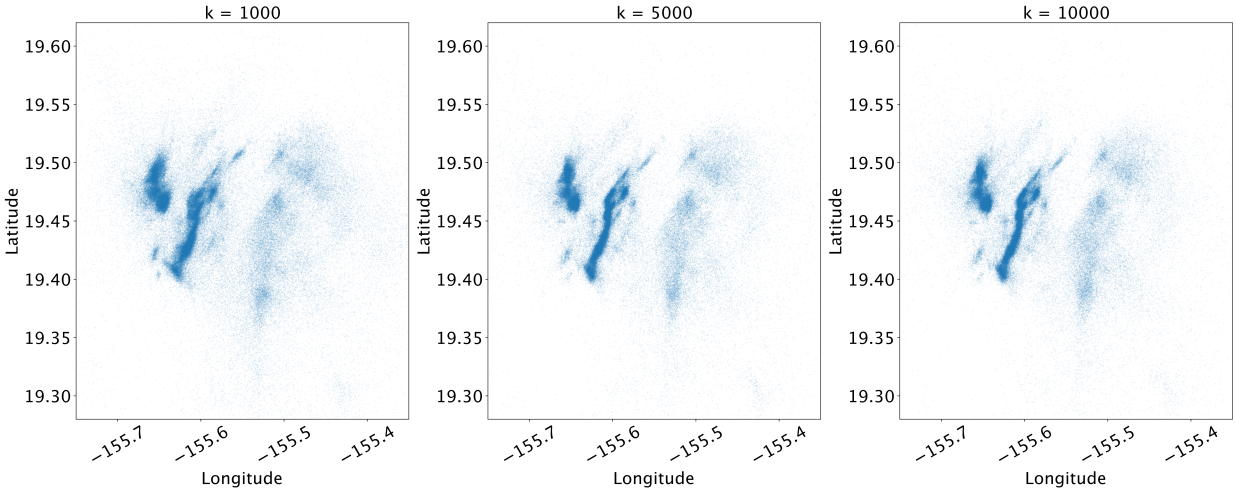

Figure S2. Earthquake location results using k-NN-based SSST calculations for varying values of the parameter k. Earthquake location resolution increases with k up to k = 5000; locations do not visibly improve with k > 5000.

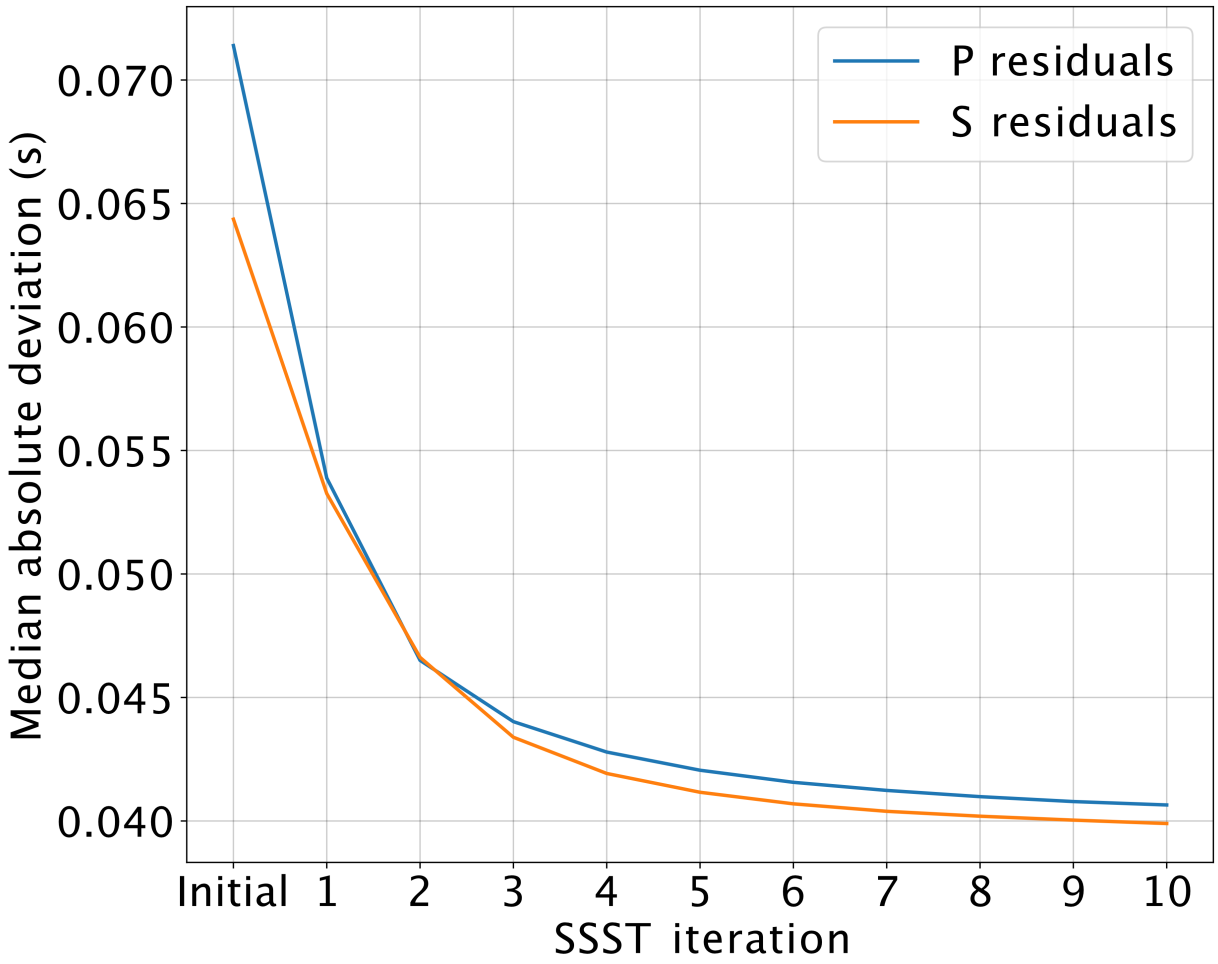

Figure S3. The median absolute deviation (MAD) of P- (blue) and S- (orange) wave travel time residuals over successive SSST iterations. The "initial" step represents travel-time residuals after the removal of outlier picks with travel-time residuals > 0.49 s, but prior to applying any SSST corrections. MAD values decrease smoothly up to iteration 10 for both P and S residuals.

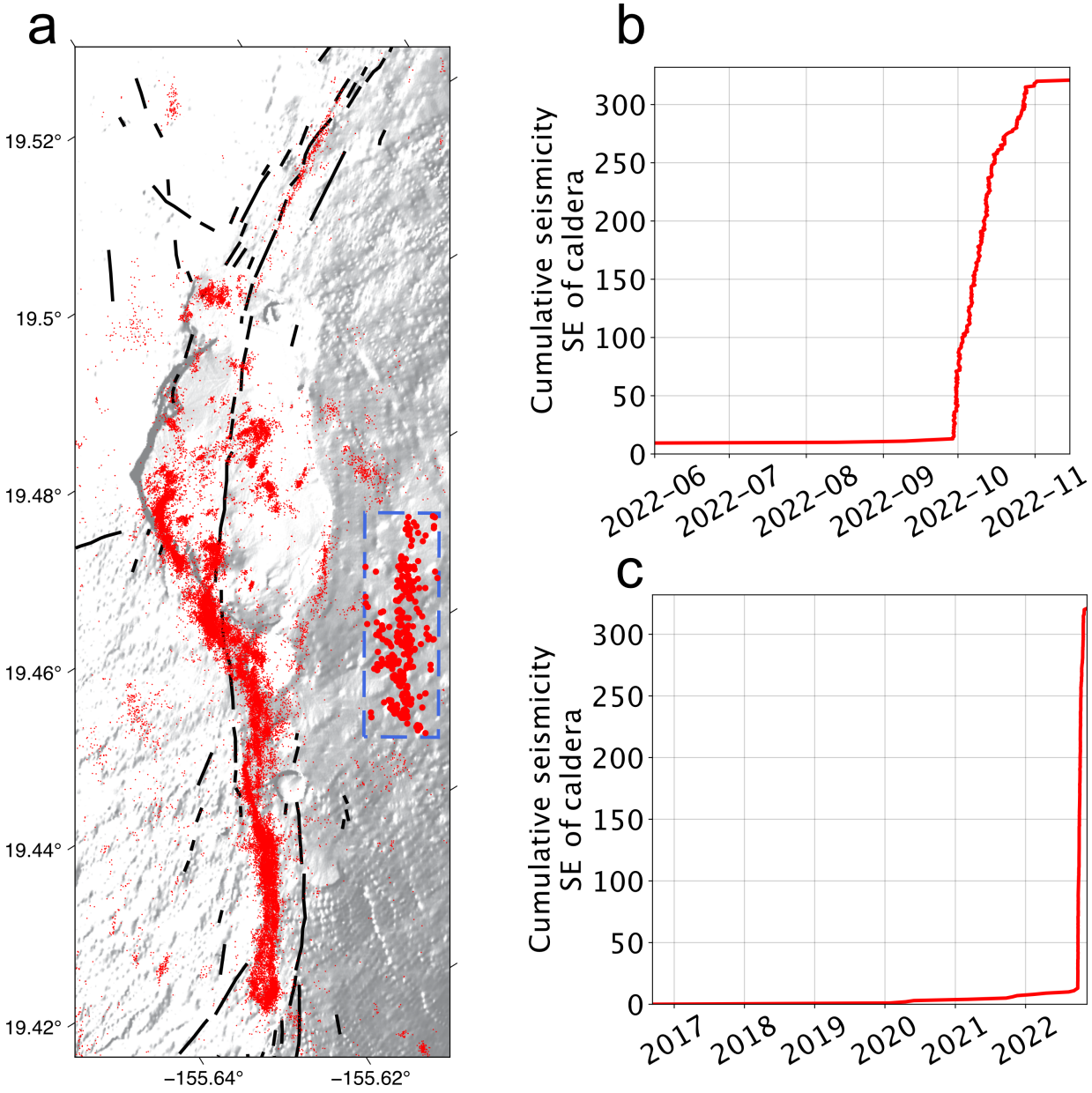

Figure S4. (a) Map view of the A-A' profile. The dashed blue box outlines a region where seismicity is quiescent until two months prior to the 2022 eruption. Black lines are mapped fissure traces (Wolfe (compiler) & Morris, 1996; Sherrod et al., 2021). Seismicity in the box is enlarged for visibility. (b) and (c) Timeseries of all seismicity in the box. The boxed region is relatively seismically quiescent until late 2022.

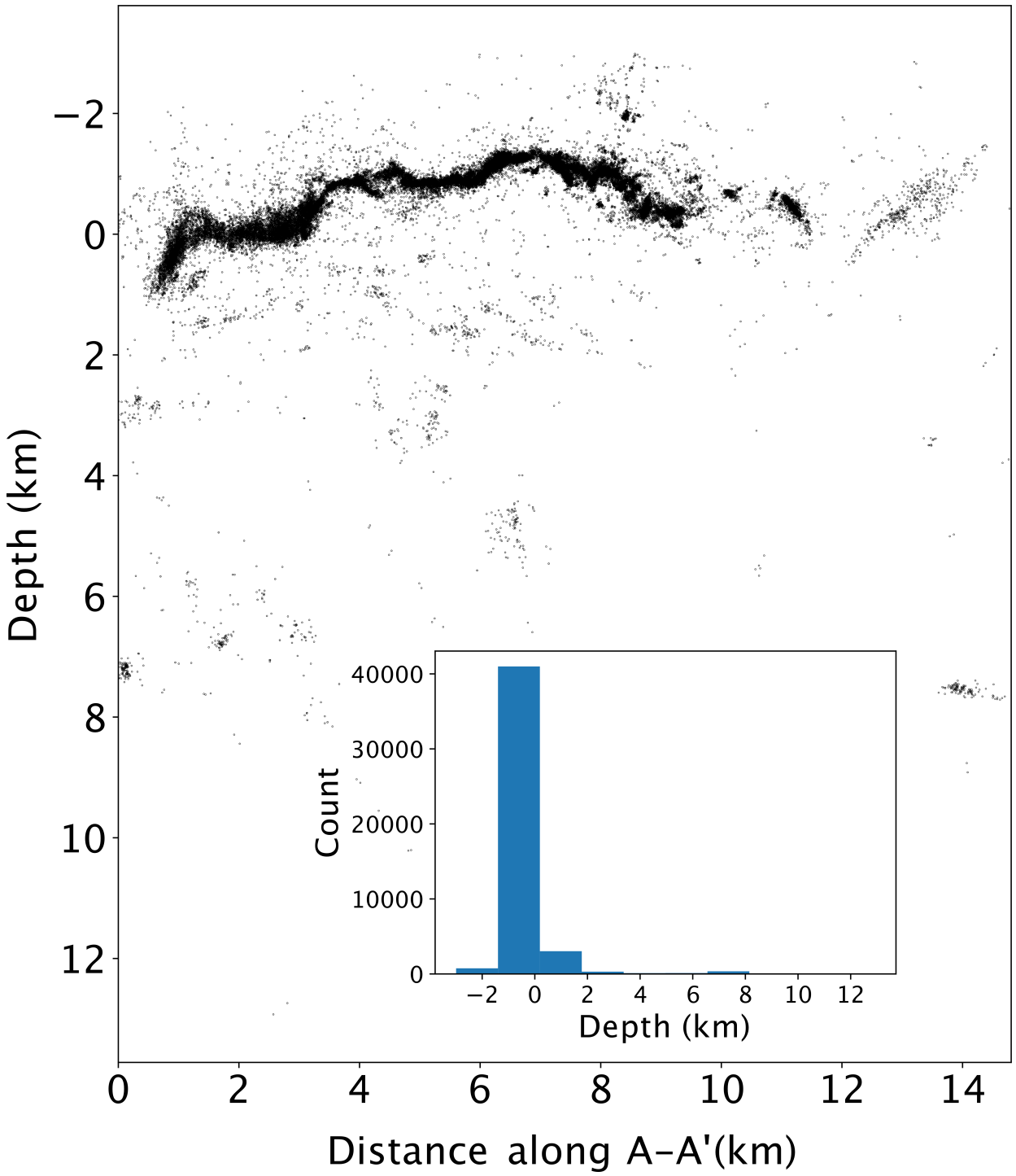

Figure S5. Depth section of seismicity along the A-A' profile down to 14 km depth. Most of the seismicity in our catalog is at or above about 1 km depth. Inset: histogram of event count by depth along the A-A' profile.

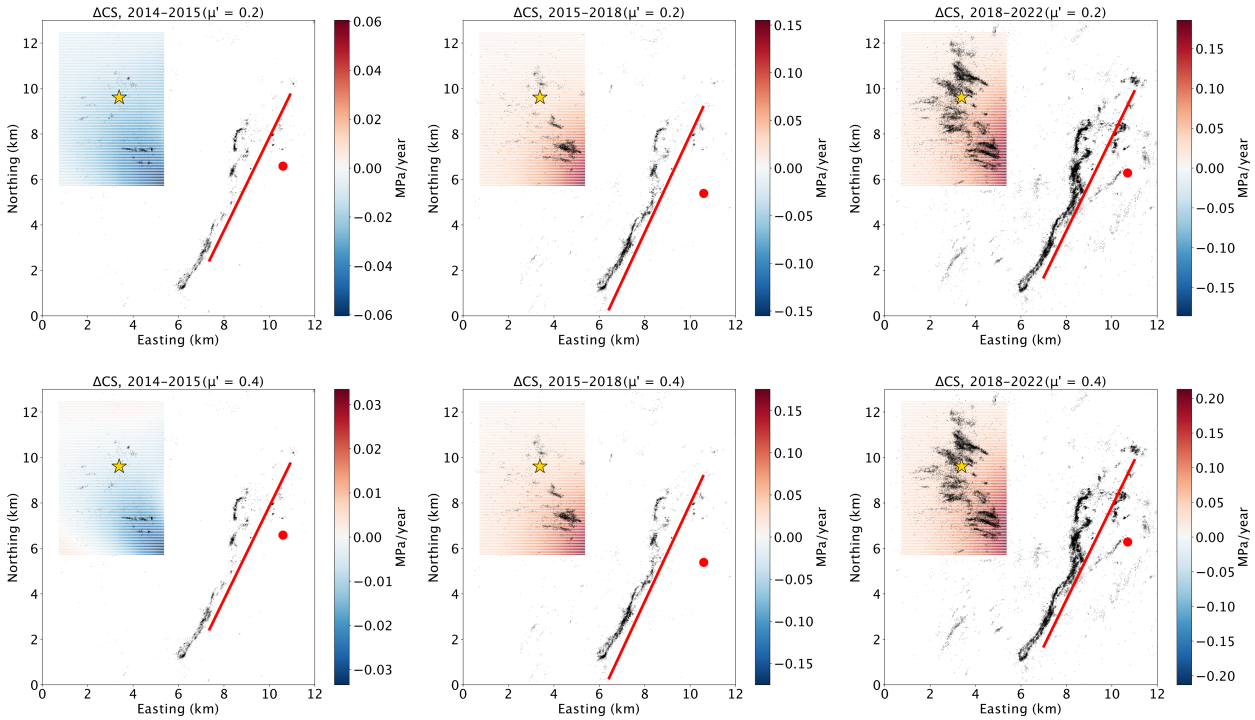

Figure S6. Coulomb stressing rates calculated on the NWF receiver plane for three different time periods and two different values of μ'. The red dot and red line represent the Mogi source and the opening dislocation source of Varugu and Amelung (2021), respectively, for each time period. Our results are qualitatively similar for $0.2 \geq \mu' \geq 0.4$.

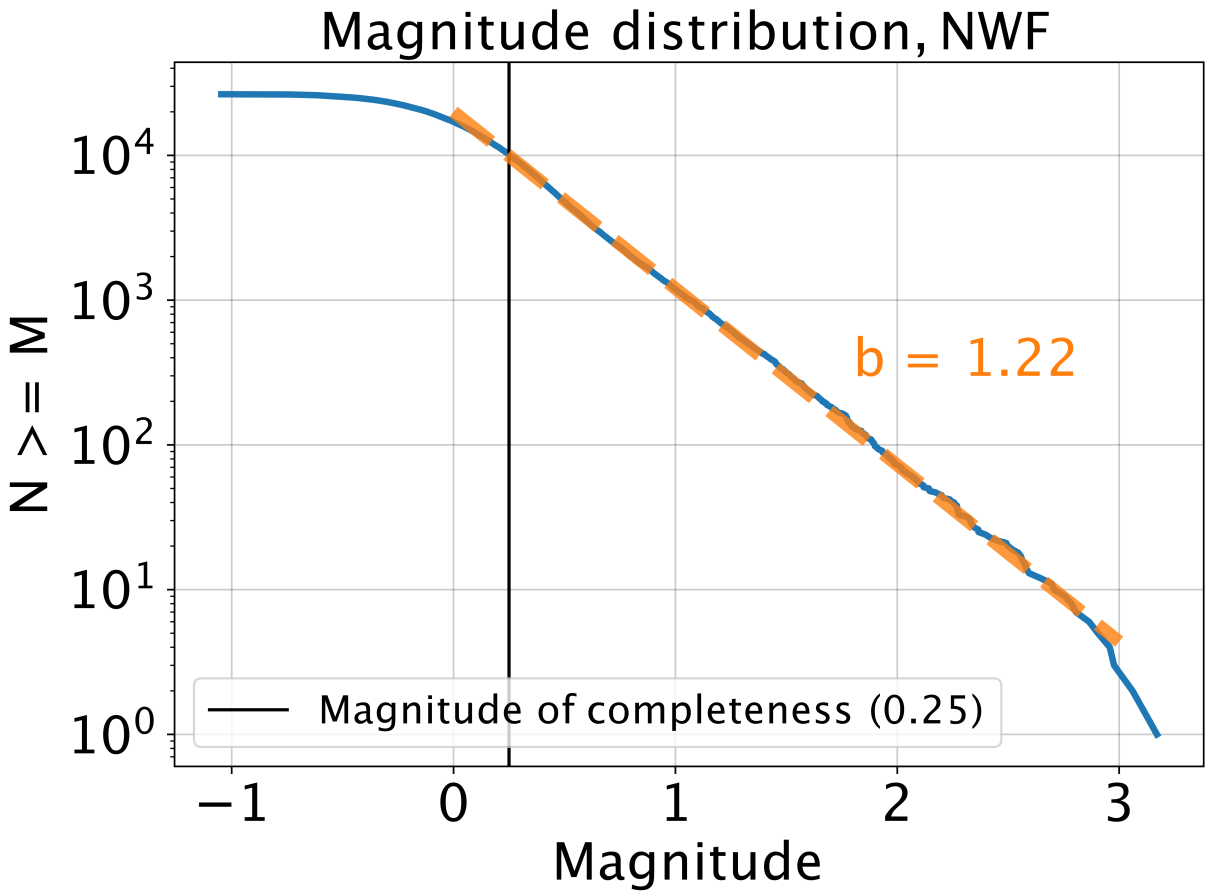

Figure S7. Cumulative magnitude distribution of seismicity within the NWF region. We estimate a magnitude of completeness for the region of 0.25.

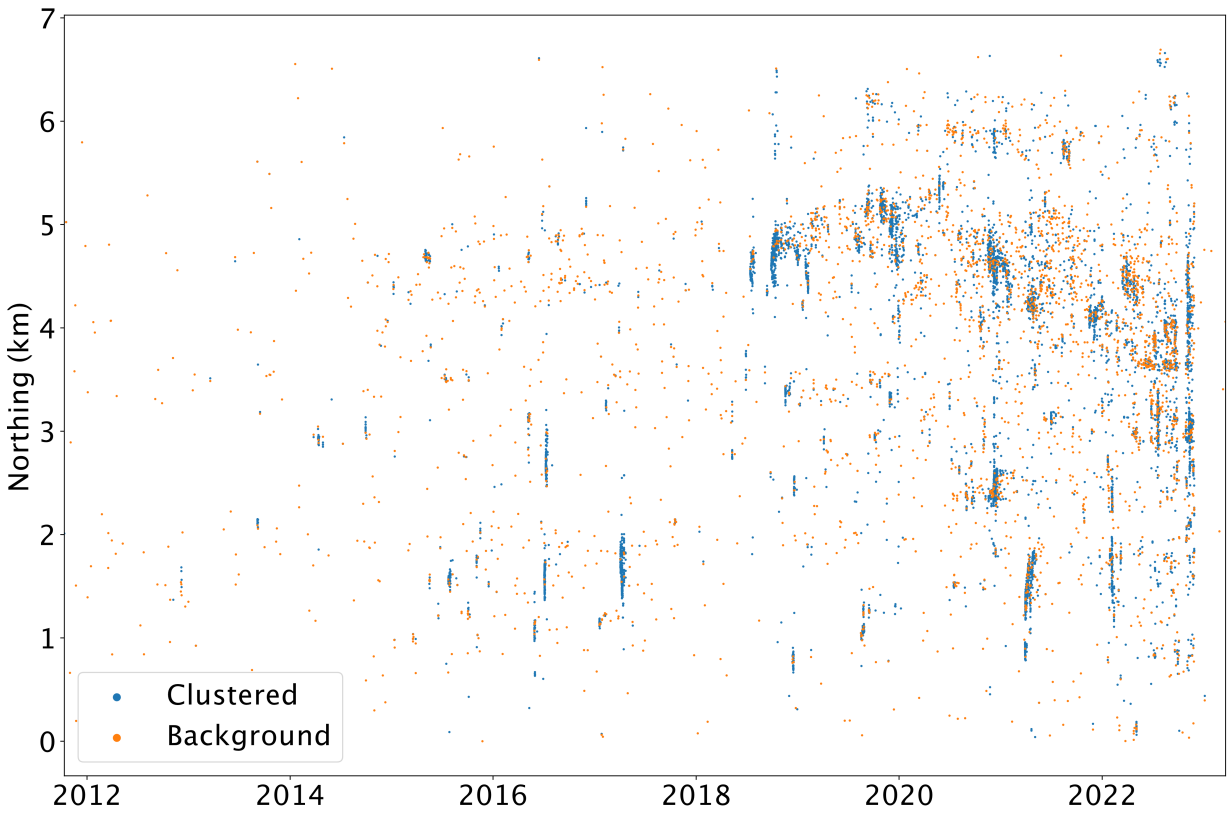

Figure S8. Time history of clustered (blue) and background (orange) seismicity in the NWF, as determined by the declustering algorithm of Zaliapin and Ben-Zion (2013). The background seismicity defines the declustered catalog.